New HST data and modeling reveal a massive planetesimal collision around Fomalhaut

András Gáspár[a,1] and **George H. Rieke**[a]

[a]Steward Observatory, The University of Arizona, Tucson, AZ 85719

Edited by Neta A. Bahcall, Princeton University, Princeton, NJ, and approved January 15, 2020 (received for review July 19, 2019)

The apparent detection of an exoplanet orbiting Fomalhaut was announced in 2008. However, subsequent observations of Fomalhaut b raised questions about its status: Unlike other exoplanets, it is bright in the optical and nondetected in the infrared, and its orbit appears to cross the debris ring around the star without the expected gravitational perturbations. We revisit previously published data and analyze additional Hubble Space Telescope (HST) data, finding that the source is likely on a radial trajectory and has faded and become extended. Dynamical and collisional modeling of a recently produced dust cloud yields results consistent with the observations. Fomalhaut b appears to be a directly imaged catastrophic collision between two large planetesimals in an extrasolar planetary system. Similar events should be very rare in quiescent planetary systems of the age of Fomalhaut, suggesting that we are possibly witnessing the effects of gravitational stirring due to the orbital evolution of hypothetical planet(s) around the star.

extrasolar planets | circumstellar disks | directly imaged planets

The simultaneous announcements of images of massive planets around Fomalhaut (1) and HR 8799 (2) were a benchmark in our exploration of exoplanets. The HR 8799 system has indeed become the prototype for complex systems of very massive planets and has been the subject of many studies of such objects (e.g., refs. 3–7). However, Fomalhaut b has been enigmatic.

An issue with the massive planet hypothesis for Fomalhaut b was the nondetection with the Infrared Array Camera (IRAC) onboard the Spitzer Space Telescope (8), which placed an upper limit of 3 Jupiter masses ($\mathrm{M_{Jup}}$) on its mass assuming an age for Fomalhaut of 200 My. A similar limit was derived from the lack of apparent perturbations in the Fomalhaut debris ring; this work favored a significantly smaller mass, e.g., 0.5 M_{Jup} (9). An upward revision of the system age to 440 ± 40 My (10) relaxed the limit from the infrared data, but a much deeper limit was obtained with Spitzer IRAC that pushed the mass limit lower. In fact, this limit appeared to be incompatible with a massive planet accounting for the visible brightness of the object (11, 12). With determination of an orbit for Fomalhaut b, it became apparent that the object would cross the ring at least in projection (13). The implications on the ring structure placed a tentative limit on the mass of Fomalhaut b as low as an Earth mass (14).

Given that the bright optical signature of Fomalhaut b seems not to be light scattered from a giant planet, a number of alternative hypotheses have been proposed, e.g., light scattered by a circumplanetary ring system (1) or by a dust cloud associated with a relatively low-mass planet (e.g., refs. 11, 15, and 16). A tentative finding that the image of Fomalhaut b might be extended was interpreted to support the dust cloud hypothesis (17); however, it was suggested that this effect instead might be due to speckle and other noise sources (13, 18). Nonetheless, a dust cloud appears to be the most plausible hypothesis.

A number of papers have addressed the origin of this hypothetical dust cloud (15, 17–19). Ref. 15 suggested that collisions among a swarm of satellites around a planet could be responsible and showed that certain models of this process lie within the constraints from assuming that the phenomenon has persisted for the life of the star and that the image is point-like. Ref. 20 found that satellite swarms around planets of mass 10 to 100 $\mathrm{M_{Earth}}$ that have evolved for 100 to 400 My could match the properties of Fomalhaut b. Ref. 17 suggested that the object could consist of dust created in the collision of two modest-sized (50 km) planetesimals similar to members of the Kuiper Belt. Ref. 18 analyzed three possible origins for the required dust cloud: 1) a giant planetesimal impact, 2) material captured from the prominent debris disk of the star, or 3) dust generated in a collisional cascade from a massive cloud of satellites around a recently formed planet. The first possibility was judged to be unlikely to reproduce the observations (21). The other two possibilities are constrained significantly by the assumption that the dust system should persist in a state similar to its present one for the main sequence lifetime of the star, i.e., ∼400 My. Ref. 19 suggested a possible solution to the lifetime issues by attributing the source to a transient dust cloud produced by a collision between planetesimals interior to the main debris belt around the star.

We report that Fomalhaut b has grown in extent and faded since its discovery in Hubble Space Telescope (HST) images from 2004, with motion consistent with an escaping trajectory. This behavior is consistent with expectations for a dust cloud produced in a planetesimal collision and dispersing dynamically. As the cloud disperses, its surface brightness has dropped, making it less prominent in the most recent images.

Significance

Although originally thought to be a massive exoplanet, the faintness of Fomalhaut b in the infrared and its failure to perturb Fomalhaut's debris ring indicate a low mass. We use all available data to reveal that it has faded in brightness and grown in extent, with motion consistent with an escaping orbit. This behavior confirms suggestions that the source is a dispersing cloud of dust, produced by a massive collision between two planetesimals. The visible signature appears to be very fine dust escaping under the influence of radiation pressure. Such events should be rare in quiescent planetary systems at the age of Fomalhaut, suggesting increased dynamical activity within the system possibly due to orbital migration of hypothetical planets.

Author contributions: A.G. and G.H.R. designed research; A.G. performed research; A.G. contributed analytic tools; A.G. analyzed data; and A.G. and G.H.R. wrote the paper.

The authors declare no competing interest.

This article is a PNAS Direct Submission.

Data deposition: The raw observational data can be downloaded from the Mikulski Archive for Space Telescopes (MAST) website maintained by the Space Telescope Science Institute (STScI). Our modeling code, DiskDyn, can be downloaded from https://github.com/merope82/DiskDyn.

[1] To whom correspondence may be addressed. Email: agaspar@as.arizona.edu.

This article contains supporting information online at https://www.pnas.org/lookup/suppl/doi:10.1073/pnas.1912506117/-/DCSupplemental.

Archival Data

Fomalhaut b has been observed only in scattered light and only with HST. The stable optical system of HST and the lack of atmospheric disturbance enable high-contrast imaging at visible wavelengths with the aid of coronagraphs. Fomalhaut b was discovered in images taken with the Advanced Camera for Surveys (ACS) coronagraph in 2004 and 2006 (1). The failure of the high-resolution channel (HRC) (which included the coronagraph) of ACS in 2007 led to the Space Telescope Imaging Spectrograph (STIS) becoming the single coronagraphic instrument onboard HST; thereafter the monitoring of Fomalhaut b continued with STIS. Images of Fomalhaut b taken with STIS in 2010 and in 2012 have been published by ref. 13.

The coronagraphs in these instruments differ in design and performance. The ACS Lyot coronagraph was located in the aberrated beam of the telescope. This limited the performance of the coronagraph at smaller $(\leq 3'')$ inner working angles. However, it was able to observe using a suite of optical filters. The STIS coronagraph is located in the corrected beam; however, it is unfiltered and therefore detects photons from 0.4 to 1 μm. While this yields high sensitivity, it also limits the fidelity of the chromatically dependent point spread function (PSF) of the telescope, which must be observed close in time to the target star because of temporal drifts in the image shape.

Since 1999, 11 HST coronagraphic programs observed Fomalhaut, either with ACS or with STIS. Of these, only 7 were true high-contrast imaging, multiorbit, and multirotation-angle programs as described in Table 1; the remaining 4 programs took only a single or a few images. Here, we describe the previously unpublished 2013 and 2014 observations of Fomalhaut b and provide a coherent and independent rereduction and analysis of all of the useful HST data.

Rereduction of Archival ACS Data. Three of the 11 HST coronagraphic programs used ACS (PI: Paul G. Kalas) and provided the discovery images of Fomalhaut b (1). We first give a brief description of the observations and the observing techniques employed within these observations. We then describe our rereduction of these data, carried out so all of the available photometry is treated identically.

Each ACS program observed Fomalhaut and Vega at multiple roll angles, the latter star to define the PSF. While Vega and Fomalhaut are not exact color matches, the response of the system through color filters to each source was approximately the same. Various length exposures were taken of each source to enable imaging of the inner and outer regions without saturation and to high signal-to-noise ratios.

The publicly available data for these observations were obtained from the Space Telescope Science Institute (STScI) Mikulski Archive for Space Telescopes (MAST) website. We downloaded corrected (_drz.fits) files, which rectify the non-square pixels of the HRC detector and also correct the field distortions. In our reductions, we rejected observations with issues such as poor centering on the coronagraph and also combined measurements in the same filter taken sufficiently closely in time that the relative motion of Fomalhaut b is insignificant (GO9862 and GO11818).

Over an orbit, the *Hubble Space Telescope* undergoes thermal expansions (a.k.a. "breathing"), which vary the PSF. Additionally, the ACS coronagraph transmits a small fraction of the occulted flux; the transmitted PSF depends on the total count received. Therefore, the ACS observations were target-PSF paired based on exposure length and interorbit sequence. PSF subtraction residuals can become substantial if target observations are not registered to ≤ 0.1 px with their PSFs. We determined the shifts between each image and its chosen PSF by observing the subtraction residuals by eye. Using the software IDP3, we registered the images well within 0.1 px by minimizing the radial streak pattern over a radius of $10''$ from the occulter. We also registered the shifts between the target images in a similar manner. We found an average offset in x and y pixel coordinates of $\Delta x = -0.32 \pm 0.21$ and $\Delta y = 0.35 \pm 0.422$, which is close to the nominal quarter pixel value given in the Instrument Handbook for pointing precision. The fluxes of the PSFs were scaled for each pairing by determining the background levels at the edges of the fields.

To pinpoint the location of Fomalhaut, which then defines the derotation center of the images, we determined the rotational symmetry origin of each image. To do so, we rotated each image by 180° and subtracted it from its original version. Subtraction residuals within the occulting spot became apparent at $\sim\pm1$-px offsets. We use this value, along with the rotational angles of individual images and the full-width at half-maximum (FWHM) of the target PSFs, to estimate astrometric errors. Following PSF subtraction, subtraction masking, and derotation, the individual target images were combined.

(Re)Reduction of Archival and Additional STIS Data. Four programs using STIS employed a multiroll/multiorbit observation technique (PI: P. Kalas for all of them), which is necessary to achieve high-contrast imaging. The results from the first two programs have been published (13); here we publish the results of the last two. As STIS is unfiltered for coronagraphic imaging, precise color matching of the PSF source is critical. Since well-matched PSF calibrators may not be available nearby, it is common to employ the angular differential imaging (ADI) technique, where a star becomes its own PSF calibrator by combining images of it taken at different roll angles. This approach works well for

Table 1. Multiroll HST coronagraphic observations of the Fomalhaut system

Program ID	Date	Instrument	Filters	Apertures	$N_{\rm Images}$	$N_{\rm Rotations}$	PSF
GO9862*	2004-05|08	ACS	F814W	CORON1.8	5	2	Vega
GO10390*	2004-10	ACS	F606W, F814W	CORON1.8	32	3	Vega
GO10598*	2006-07	ACS	F435W, F606W, F814W	CORON1.8, CORON3.0	53	4	Vega
GO11818*	2010-06|09	STIS	N/A	WEDGEB2.5[†]	19	7[‡]	ADI
GO12576*	2012-05	STIS	N/A	WEDGEB2.5	48	12[‡]	ADI
GO13037	2013	STIS	N/A	WEDGEB2.5	48	12[‡]	ADI
GO13726	2014	STIS	N/A	WEDGEB2.5[†]	24	8	Vega and ADI

Programs marked with "ADI" were planned to use angular differential imaging and therefore did not observe a PSF source. 05|08, May|August; 10, October; 07, July; 06|09, June|September; 05, May.

*Previously published data.

[†] Observations were also taken at additional apertures (BAR10 for GO11818 and BAR5 for GO13726), but were not included due to low S/N at the position of Fomalhaut b.

[‡] The majority of rotations were separated by only a few degrees $(\leq 25^\circ)$.

edge-on or inclined narrow-belt disk systems, such as that of Fomalhaut.

The STIS coronagraph consists of two occulting wedges and two occulting bars. The GO11818 program observed Fomalhaut in 2010 using the 2.5″-wide position on the "B" wedge. Deeper images at the same occulting position were obtained in 2012 (GO12576) and 2013 (GO13037) using additional roll angles (for a total of 12), which helps to suppress PSF subtraction residuals as well as establishing a better PSF for ADI. The 2014 observations (GO13726) integrated for a slightly shorter time, but the STIS observations are contrast and not photon limited, so the data are still adequate for the detection of Fomalhaut b.

The reduction of the STIS data followed similar steps to those for the ACS data. The level of geometric distortion for STIS is minimal; the largest offset near the location of Fomalhaut b is at most 0.5 px, based on available distortion maps (22). For high-quality astrometric measurements, however, subpixel alignment precision is necessary. Therefore, we opted to download and analyze the distortion-corrected images (_sx2.fits). Each of the images was used to generate its own mask, based on the underlying STIS occulter mask and generous saturation masking at 75% of the full well value. We used the same methods as for the ACS data to measure the offsets among all images within an observation program. The tracking of radial subtraction patterns and their minimization by eye allowed us to define shifts in both pixel coordinates within 0.1 px. As the STIS occulters are not transparent, its coronagraphic PSF is more stable than that of ACS, and the radial patterns remain generally the same for the complete observing program. This enables high-precision registering of all data to the same coordinates. We did, however, notice small interorbit variations and therefore decided to construct PSFs for each exposure sequence ID, median combining all first, second, etc., images of all orbits. This method follows the ADI technique, but also folds in the thermal changes to the HST optical telescope assembly (OTA).

The Lyot stop for the STIS coronagraph blocks only light from the edges of the OTA; therefore, the diffraction spikes are prominent in the images and only the wings of the PSF are suppressed. While this necessitates additional masking during image processing and reduces the imaging real estate, it also allows precise locating of the central star for image derotation. Following image registering with PSF subtraction residuals, the location of the star (determined by tracking the diffraction spikes) has a remarkably small error of 0.12 px (6 mas) in both coordinates. As for the ACS images, following PSF subtractions, masking, and derotation, the individual images were combined.

In Fig. 1, we show the results of our image reductions and analysis, including a high signal-to-noise combined STIS image and detailed snapshots of Fomalhaut b at all epochs.

Astrometry and Photometry of Fomalhaut b

Determining the astrometric location of Fomalhaut b in the ACS and STIS images started from the published coordinates (13) in the 2004, 2006, 2010, and 2012 images and was based on forward projections for the 2013 and 2014 images. While the source is clearly identifiable in the F606W ACS and the 2010 and 2012 STIS images, it is more difficult to pinpoint it in the others. For

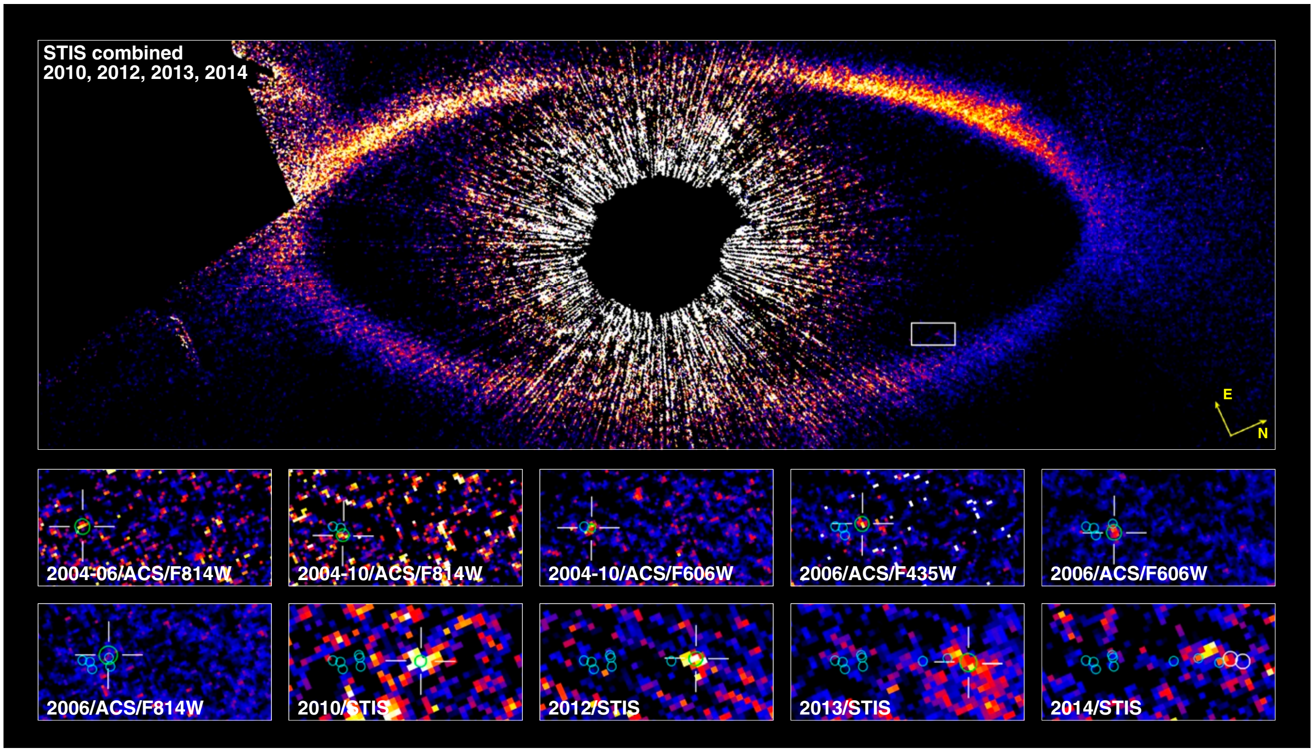

Fig. 1. (*Top*) Median combined image of all multiroll STIS observations (2010, 2012, 2013, and 2014) of the Fomalhaut system. Fomalhaut b is visible in the image within the white rectangle, which is 2″ × 1″ in size and highlights the area shown in the postage-stamp images below. The postage-stamp images show the individual observations (see text for descriptions of each). The individual images are scaled to the same level per filter [0 to 0.1 counts per second ($\text{cts}\cdot\text{s}^{-1}$) for the F606W and F435W ACS filter and for STIS and 0 to 0.05 $\text{cts}\cdot\text{s}^{-1}$ for the F814W ACS filter]. The green circles with crosses highlight the then current positions of Fomalhaut b, with 3σ astrometric error radii, while the smaller cyan color circles show the previous positions, to highlight the spatial motion of the source. For the 2014 image, we show the two locations predicted by the two independent trajectory fits. The bright spot "near" the predicted locations is too far to be considered associated with Fomalhaut b.

Table 2. Astrometry of the Fomalhaut b object

Date	Instrument	ΔR.A. (″)	Δδ (″)
2004/06	ACS (F814W)	−8.542 ± 0.021	9.144 ± 0.021
2004/10	ACS (F606W)	−8.580 ± 0.011	9.198 ± 0.011
2004/10	ACS (F814W)	−8.642 ± 0.017	9.194 ± 0.018
2006/07	ACS (F435W)	−8.614 ± 0.020	9.363 ± 0.020
2006/07	ACS (F606W)	−8.683 ± 0.021	9.341 ± 0.021
2006/07	ACS (F814W)	−8.590 ± 0.025	9.364 ± 0.026
2010/09	STIS	−8.850 ± 0.016	9.824 ± 0.016
2012/05	STIS	−8.915 ± 0.019	10.024 ± 0.020
2013/05	STIS	−9.018 ± 0.027	10.173 ± 0.025
2014/09	(Bound model)	−9.029*	10.273*
2014/09	(Cloud model)	−9.093*	10.360*

*Projected location of the source (no detection). 06, June; 10, October; 07, July; 09, September; 05, May.

the F435W and F814W images, we searched for peaks near the F606W positions, while for the 2013 STIS image forward projections from the previous epochs aided in locating the source. We calculated the locations using the centroiding algorithm in the Image Reduction and Analysis Facility (IRAF) software, DAOPHOT.APPHOT, initiated on the brightest pixel within a 2-px radius of the predicted locations. The object is visibly expanding in size in the STIS dataset and therefore its astrometric position has an increasingly larger error. The object was not detected in the 2014 dataset at either model trajectory location. All peaks visible in the 2014 dataset are spatially far enough from any realistic trajectory projection that they can be dismissed. The astrometric positions are summarized in Table 2 and plotted in Fig. 2.

The astrometric errors are calculated as the root sum squares of the derotational errors and the PSF FWHM astrometric errors. The derotational errors in right ascension and declination were calculated for each individual observation, based on the derotation angles within each observation set and the precision of image centering, weighted by the exposure time of each individual image. We calculated the derotational errors with a Monte Carlo code. The centroiding astrometric errors were calculated based on the standard formula of

$$\sigma_{\text{centroid}} = \frac{1}{2.355}\frac{\text{FWHM}}{\text{SNR}}, \qquad [1]$$

where SNR gives the peak pixel signal to background pixel noise ratio. Centroiding FWHMs were provided by IRAF for both right ascension and declination.

We performed aperture photometry of Fomalhaut b in all of the final reduced images. The photometry was performed with a 2.1-px radius aperture. The background was measured in 2.1-px radius apertures randomly placed at the same stellocentric distance as the target source (avoiding areas where the disk is prominent). The photometry error was determined as the SD of these background measurements. This is the same method that ref. 13 used to estimate the background and photometry errors. We applied aperture corrections of factors of 3.03, 2.56, 2.27, and 1.45 for the ACS (F814W, F606W, F435W) and STIS observations, respectively, based on TinyTim theoretical PSFs (23), which include broadening due to the Lyot stops.

We summarize our photometry compared to previously published values in Table 3. The instrumental flux values (counts·s^{-1}) were converted to various physical flux units using synphot, assuming the incident light that is scattered has a spectral distribution identical to that of the host star (A3V) and using conversion factors appropriate for the instrument setup and observation date. The pivot wavelength of the instrument/filter setup was used to calculate the Jansky (Jy) units. Our photometry values are generally in agreement with the previously published values for the ACS data, except for the single observation in the F435W filter. For STIS, our photometry agrees with that of ref. 13; however, it is fainter than that of ref. 17 by a factor of 2. Such discrepancies have been noted in the literature for this source and are likely an outcome of differences in data reduction and photometry methods. Nevertheless, the general conclusions of our paper are not affected by these discrepancies because we have applied identical procedures to all of the images.

The object fades in each individual band over time; however, there is a color shift between the various ACS filters and an

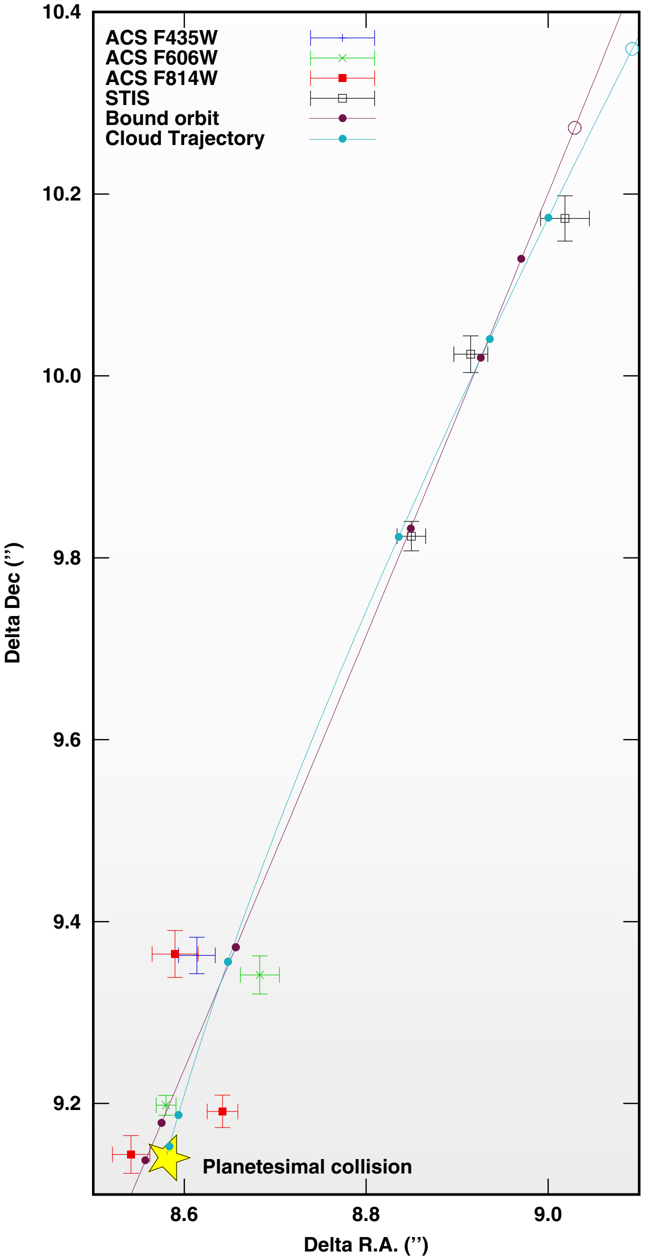

Fig. 2. Astrometry of Fomalhaut b (see text for details). The circles show the projected location of the object in 2014 for both the bound orbit and cloud models. The purple line and dots give the best-fitting bound orbit and locations for each observation, while the cyan line and dots give the same for the dust cloud model.

Table 3. Photometry of the Fomalhaut b object

Date	Filter	F (cts·s^{-1})	F (Jy)	m_{Vega}	m_{AB}	F_{prev}
2004/06	F814W	0.65 ± 0.16	3.83e-7	24.51	24.94	N/A
2004/10	F606W	1.70 ± 0.22	5.23e-7	24.51	24.61	24.43 ± 0.08 mag (1); 24.92 ± 0.10 mag (16); 6.3 ± 1.0 $\times 10^{-7}$ Jy (17)
2004/10	F814W	0.72 ± 0.23	4.23e-7	24.40	24.83	N/A
2006/07	F435W	1.28 ± 0.26	8.90e-7	24.11	24.03	25.22 ± 0.18 (16); 3.6 ± 0.9 $\times 10^{-7}$ Jy (17)
2006/07	F606W	1.52 ± 0.15	4.71e-7	24.63	24.72	25.13 ± 0.09 mag (1); 24.97 ± 0.09 mag (16); 4.3 ± 0.6 $\times 10^{-7}$ Jy (17)
2006/07	F814W	0.56 ± 0.08	3.24e-7	24.69	25.12	24.55 ± 0.13 mag (1) 24.91 ± 0.20 mag (16); 3.6 ± 0.7 $\times 10^{-7}$ Jy (17)
2010/09	Clear	0.77 ± 0.10	3.58e-7	24.77	25.02	0.49 ± 0.14 cts·s^{-1} (13); 6.1 ± 2.1 $\times 10^{-7}$ Jy (17)
2012/05	Clear	0.58 ± 0.10	2.71e-7	25.07	25.32	0.50 ± 0.11 cts·s^{-1} (13)
2013/05	Clear	0.47 ± 0.08	2.17e-7	25.32	25.56	N/A
2014/09*	Clear	0.32 ± 0.14	1.48e-7	25.73	25.97	N/A
2014/09†	Clear	0.23 ± 0.14	1.07e-7	26.09	26.33	N/A

06, June; 10, October; 07, July; 09, September; 05, May.

*Flux at the predicted location of the source using the bound orbit trajectory.

†Flux at the predicted location of the source using the unbound cloud model trajectory.

offset between the ACS and STIS data in general. The color shift is a natural consequence of the dust cloud being slightly bluer than the central star. The offset between the ACS and STIS data is most likely an artifact, brought on by the combination of changes in two variables: 1) The source becomes extended over time and 2) the STIS photometry aperture is physically larger than the ACS one, due to the larger projected pixel sizes of the detector (Fig. 3 legend). The precision alignment of the STIS data and lack of any higher signal points near the predicted location of the source (even with a wide margin of astrometric error) give high confidence to our nondetection in 2014.

Interpretations of the Observations

We draw three basic conclusions about Fomalhaut b from the observations: 1) It is probably moving out of the system, 2) it has become increasingly extended, and 3) it has faded below our detection limits. We support these conclusions first by comparing bound and unbound fits to the observed motion of the object. We then analyze its evolution in size and brightness using a model providing a self-consistent explanation of all three unique aspects of its behavior.

Bound Orbit of Fomalhaut b. If the underlying object for Fomalhaut b is planetary, it should be following a stable bound orbit. To fit the best solution for such an orbit and its joined Bayesian errors, we used a Markov chain Monte Carlo (MCMC) fitting routine (24). Orbital solutions were projected forward to each epoch from the orbital point closest to the first observation location. We assumed uniform priors on the orbital elements (semimajor axis a, eccentricity e, inclination ι, argument of periapsis w, right ascension of the ascending node Ω) and determined their statistics using 5,000 steps following a burn-in limit of 2,000 steps for 6,000 test chains. These orbital elements are defined in the plane of the Fomalhaut disk (assuming a system position angle of 336° and inclination of 66°). In Fig. 4, we show the results.

In Fig. 2, we also plot (with purple color) the best orbital solution (at the reduced χ^2 minimum, given in the Fig. 4 legend), assuming this stable bound orbit. Although the observations lie near the track of the "best" orbit, the positions along that track do not agree with the observations within errors. This issue is prominent for 2013, the point to the upper right, where the observed position is significantly ahead of the bound orbit prediction (purple dot, Fig. 2), consistent with the object experiencing nongravitational acceleration directed away from the star. A planetary body would also not explain the fading and extent of the image. Therefore, additional models of the motion and behavior of the source are necessary.

Fomalhaut b as a Dynamically Dissipating Collisional Dust Cloud. We now consider an alternative model tracing the evolution of the system through the following steps: 1) Two large (≥100 km in radius) asteroids collide catastrophically; 2) the collision fragment sizes follow a power-law distribution down to the submicrometer level; 3) the fragments inherit random velocities, resulting in the expansion of the dust cloud relative to the center of mass (COM) of the colliding asteroids; and 4) the final trajectories depend on fragment size: larger ones unaffected by radiative forces will undergo Keplerian shear, while the smaller ones will converge onto radial trajectories and leave the system. The surface area of the dust cloud observed in scattered light is dominated by the submicrometer particles that are leaving the system. The apparent motion of the observed image should reflect such motion.

To test this scenario, we modeled the dynamical evolution of such a hypothetical system using our code DiskDyn. Developed to model the dynamical evolution of debris disks and dust clumps, DiskDyn is a complex numerical code able to include

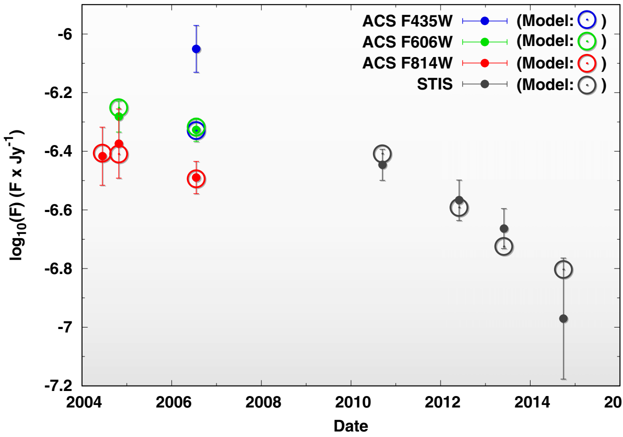

Fig. 3. The photometry of Fomalhaut b at all observed epochs and wavelengths. The error bars shown are at 1σ. The offset between the ACS and STIS data is most likely an artifact, due to the larger STIS pixel sizes, the spatial expansion of the dust cloud, and the method of photometry that was necessary. The expansion of the dust cloud over time, convolved with the HST PSF, results in the central peak brightening. This artifact is further enhanced by the larger STIS pixel size. As we had to use larger physical apertures for the STIS data than for the ACS data (same number of pixels), the object seems to brighten artificially. Identical photometry of the cloud model ACS and STIS data, shown with open circles, exhibits similar behavior.

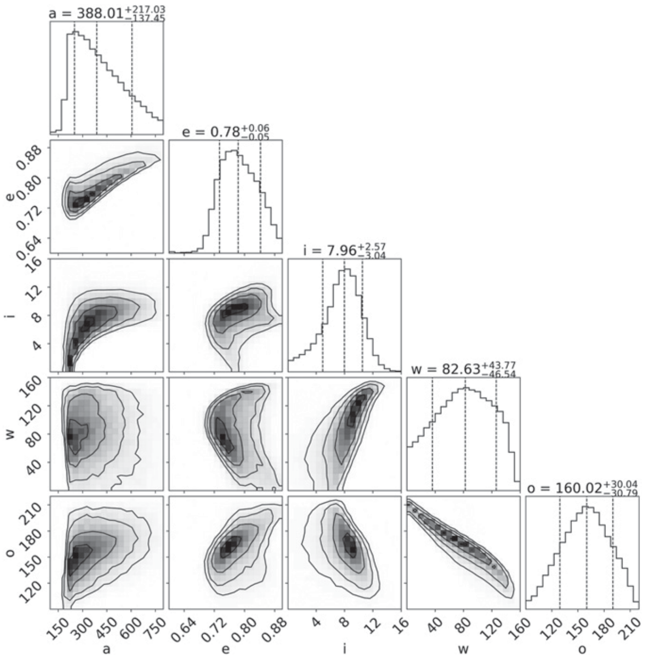

Fig. 4. Posterior probability distributions over the free orbital parameters of Fomalhaut b, assuming a stable bound orbit, using MCMC analysis (6,000 chains, 5,000 steps, burn-in limit at 2,000 steps). The diagonal panels show 1D projections (marginalized over all other parameters) of the probability density, while the off-diagonals show 2D projections of the correlations between parameters. The mean and the 1σ levels of the 1D projections are shown, while the global reduced $\chi^2 = 3.18$ minimum of the distribution is at $a = 385.5$ au, $e = 0.7604$, $\iota = 9.90°$, $w = 118.00°$, $\Omega = 139.59°$. In *SI Appendix*, Fig. S1, we show the chains of our MCMC analysis.

the effects of gravitational, radiative, and magnetic forces on dust particles, as well as calculate the gravitational effects of a large number of massive bodies. Additionally, DiskDyn provides .fits images of the scattered light and thermal emission from the dust particles and complete SEDs. Due to the numerically intensive calculations, DiskDyn runs on graphical processing units (GPUs).

While DiskDyn is a versatile modeling code, it does not provide fitting tools. Therefore, we first fitted the trajectory of the dust cloud in a similar fashion to that for the bound orbit solution (with MCMC) to obtain the input values for DiskDyn; however, for this fit, we did not constrain the trajectory to be bound. Instead, the launch location and velocity of the cloud were defined by its Cartesian coordinates and velocities (yielding an extra free parameter relative to the bound orbit solution). The trajectories of small dust grains are characterized by β, the ratio of radiation force to gravitational force on the particles. In Fig. 5, we show the total (thermal and scattered) flux as a function of particle size (weighted by the dust number density) at an observational wavelength of 0.6 µm, which corresponds to the wavelength observed with ACS in the F606W filter and with STIS. Fig. 5 also shows the β values, as a function of particle radius. The particle radius range most prominently observed with HST is between 0.07 and 0.7 µm, with flux peaks from dust with radii of 0.11 and 0.23 µm. These sizes have β values of 10.2 and 7.17, respectively. Therefore, for initial trajectory fitting we assumed $\beta = 10$ for all particles. However, our final DiskDyn dust cloud model calculates realistic dust optical properties [since we are concerned only with scattered light approximated by Mie theory, we used astronomical silicates only (25)] and dynamics.

Fig. 6 shows the MCMC analysis of the initial location of the planetesimal collision and launch velocity of the observed dust particles, determined in the plane of the Fomalhaut system. The only constraint on the initial condition was that the collision had to occur within 150 au of Fomalhaut. As Fig. 6 shows, two families of solutions were found, one with a sharp probability peak at $x = 91$ au and one with a broader distribution ($80 \leq x \leq 90$ au). The best fit (with a reduced $\chi^2 = 2.38$—compared with 3.18 for the best bound orbit fit) was for a collision occurring at $x = 91.24$ au, $y = -47.62$ au, and $z = -13.47$ au, with an initial launch velocity of 1.59 au$\cdot$y^{-1}, twice the Keplerian orbital velocity for a circular orbit at the location of the collision. However, solutions with velocities between 0.59 and 22.13 au$\cdot$y^{-1} (at different launch positions) produce fits with reduced χ^2 lower than the best bound orbit fit. The best-fitting trajectories were from the first family of solutions, typically having larger velocities (from 1.08 au$\cdot$y^{-1}), while the best fits from the second family of solutions yielded fits with reduced χ^2 similar to that of the bound orbit with velocities up to 0.8 au$\cdot$y^{-1} (i.e., sub-Keplerian velocities, assuming circular orbits). Trajectories originating from elliptical bound orbits were found in both families.

An additional constraint on the model is the speed at which the cloud expands. While the original launch velocity (combined with radiative forces for the dust particles) will determine the average central line of the trajectory, the collisional fragments will also diverge radially from the central line (trajectory of the COM) due to the explosive nature of the event that produced them. In Fig. 7, we show the observed evolution of the radius of the dust cloud. The observed size depends on the instrumental PSF, the pixel scale, the reduction algorithm, and observatory guiding artifacts. We estimate and correct for these in our analysis in Fig. 8. In 10 y the cloud has expanded considerably, to the point where it is larger than the HST PSF (i.e., partially resolved).

These measurements can be used to place limits on the collisional velocity that produced the cloud. Laboratory measurements have shown that the speeds of daughter particles in collisions, relative to a stationary COM, are roughly identical to the relative impact velocities (26). Due to similar orbital paths between colliding bodies, the average collisional velocities in

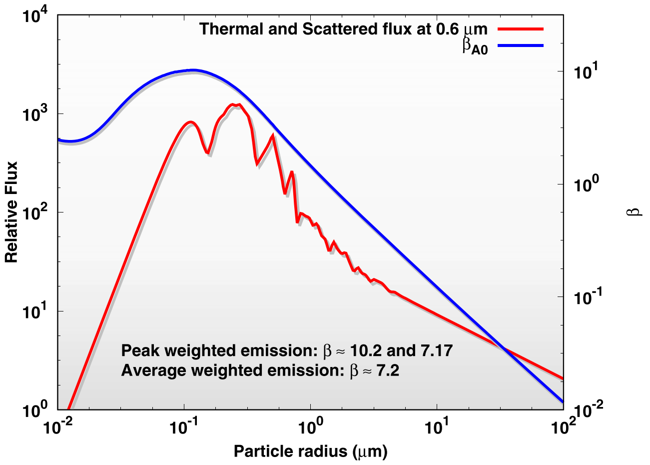

Fig. 5. The relative emission flux (thermal and scattered) at an observational wavelength of 0.6 µm (approximating the F606W ACS filter and the peak of the spectral response of the unfiltered STIS detector) as a function of particle size, assuming the modeled underlying power-law size distribution. We also plot the value of β as a function of particle size on the secondary axis for the dust particles we modeled around an A0 spectral-type star. The particles contributing most of the flux have a weighted average of $\beta = 7.2$.

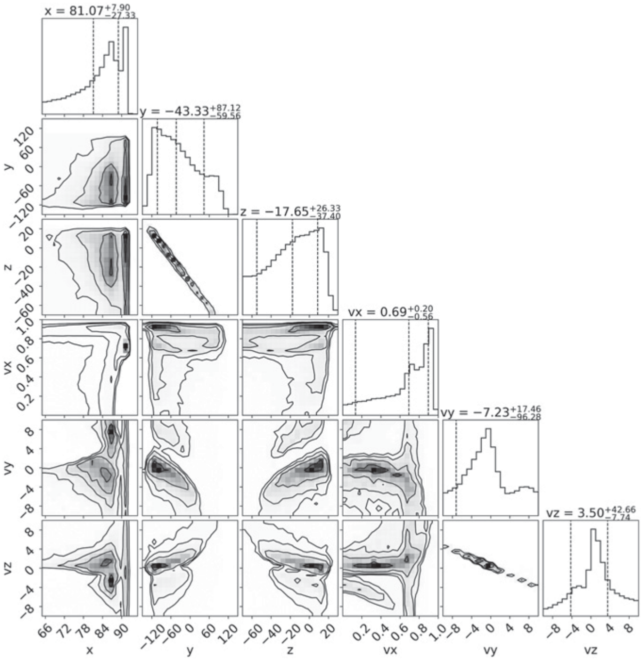

Fig. 6. Posterior probability distributions over the free orbital parameters of Fomalhaut b, assuming an unconstrained cloud model orbit, using MCMC analysis (6,000 chains, 5,000 steps, burn-in limit at 2,000 steps). The global reduced minimum of the distribution is $\chi^2 = 2.38$. The coordinates (in au) and velocities (in au·y^{-1}) are defined in the plane of the Fomalhaut system. The chains are shown in *SI Appendix*, Fig. S2.

disks are around 7.5% of the orbital velocity (27). It is unlikely that either of the colliding bodies was originally on a high-speed unbound orbit, so the daughter particles will likely acquire an additional velocity around 5 to 10% of a typical Keplerian velocity at the location of the collision, in a random direction relative to the COM. Some variation in this fraction is expected, as the collision did not happen in a disk. The inherited launch velocity of the cloud will then likely project onto a bound orbit as well. Gravitational forces will be dominant for the larger and undetected bodies, so they will remain in bound orbits and undergo Keplerian shear due to the small variations in launch velocity. However, the smallest particles (observed by HST) will experience additional radial acceleration due to radiative forces and be deflected onto unbound orbits. The expansion of the cloud is dominated by the random velocities acquired during the collision for this source.

In Fig. 8, we illustrate the expansion of the cloud. From each measured radial value, we subtract the wavelength-dependent standard deviation of the approximating Gaussian (σ) of the HST PSF ($\sigma_{\mathrm{STIS}} = 0.''033$, $\sigma_{\mathrm{F435W}} = 0.''019$, $\sigma_{\mathrm{F606W}} = 0.''026$, and $\sigma_{\mathrm{F814W}} = 0.''035$). These values include PSF broadening due to the Lyot stop of the coronagraphs and also guiding drift. The instrumental PSF broadens due to the pupil stops, which restrict the HST aperture diameter to 88.5% and 85.5% of its nominal value for the ACS and STIS detectors, respectively. Additionally, guiding HST is difficult when observing Fomalhaut and is typically done using a single guide star, possibly resulting in tracking drifts. We measured a per-orbit drift of $0.''015$, which corresponds to $0.''0015$ per exposure (2.9% of a pixel, i.e., it is negligible). The 2004 ACS images have widths approximately equal to the theoretical values; i.e., the cloud is still a point source and therefore the collision likely happened close in time to the first observations. However, the dust cloud is visibly extended in the STIS images where it is observed (2010, 2012, and 2013). The spatially extended nature of the source in the 2010 and 2012 images was also already noted by ref. 13. They give minor and major axis dimensions; if we take the geometric mean, the agreement with our radial average is within 10%. As a third independent confirmation of the extended nature of the Fomalhaut b source in the STIS images, we investigated the size of point-like background features in the raw data. A visibly slightly elongated peak, possibly the core of a background galaxy, had a fitted standard deviation of only $0.''042 \pm 0.''008$, more than two times smaller than that of Fomalhaut b. The extended Fomalhaut b source is well sampled in the STIS images at their respective epochs; therefore, pixel-scale level artifacts do not need to be considered. Following fitting, the expansion of the cloud follows a slope of 0.050 ± 0.016 au·y^{-1}, which corresponds to an orbital velocity of the colliding bodies equal to 0.5 ± 0.08 to 1.0 ± 0.16 au·y^{-1}, assuming a collisional velocity 10 to 5% of the orbital velocity, respectively. The observed expansion of the cloud, therefore, places the following constraints on the collision: 1) The collisional event happened close in time to the first observations in 2004, 2) the colliding bodies had velocities up to ∼1.2 au·y^{-1}, and 3) the final launch velocity of the cloud cannot be much higher than this value either. The best-fitting launch configuration that also conforms to these constraints has the following values: $\mathrm{x} = 91.23$ au, $\mathrm{y} = -55.97$ au, $\mathrm{z} = -9.82$ au, $\mathrm{vx} = 0.719$ au·y^{-1}, $\mathrm{vy} = 0.783$ au·y^{-1}, and $\mathrm{vz} = -0.232$ au·y^{-1}, yielding a reduced $\chi^2 = 2.48$ and a collisional event that happened 39 d prior to the first observations. This result is in good agreement with the collisional time of 2004.03 ± 0.91, predicted by the expansion. This launch position and velocity will result in a bound orbit of $\mathrm{a} = 334.4$ au, $\mathrm{e} = 0.695$, and $\iota = 12.6°$ for the larger undetected fragments of the collision. The smaller dust particles, as discussed before, will be ejected due to the influence of radiative forces. In Fig. 2, we plot their trajectory (assuming $\beta = 10$), with positions marked at each observation date.

With this best-fitting initial location and launch velocity we used DiskDyn to model the dynamical evolution of the dust cloud. Due to its larger uncertainty and importance in determining the decrease in surface brightness of the cloud, the SD of the radial expansion velocities of the dust particles was kept as a variable. A handful of models with σ_{v} between 0.05 and 0.15 au·y^{-1} were explored. We generated 10^6 dust particle tracers with a size distribution slope of $\alpha = -3.65$. This value is found to be typical of debris disks (28), and it is consistent with the value of $\alpha = -3.50$ found for particles >100 μm (to make the slope not influenced by PR drag) in zodiacal dust bands formed in the recent collisional breakup of asteroids (29). Slightly shallower but similar ($\alpha \sim -3$ to -3.3) slopes were found for the size distribution of dust sublimating off comets and in disrupted asteroids (30–32). The minimum particle size was 0.1 μm (the largest size is irrelevant, as long as all sizes that are efficient at scattering optical light are included). The total dust mass was calculated from scaling our calculations to the observations.

The DiskDyn dust cloud model was evolved on a GeForce GTX Titan Black GPU, using 0.01-y time steps. For the central star, we assumed Fomalhaut's physical parameters ($\mathrm{L} = 15.36\ \mathrm{L}_{\odot}$, $\mathrm{R} = 1.8\ \mathrm{R}_{\odot}$, $\mathrm{M} = 1.92\ \mathrm{M}_{\odot}$, $\mathrm{d} = 7.7$ pc). Dust particles from radii of 0.1 μm to 1 mm were generated in 290 logarithmically spaced size steps, with optical constants for astrosilicates (33). We performed Mie scattering calculations, taking into account the scattering angles between Fomalhaut, the dust grains, and our viewing angle of the system. The results of our modeling are also shown in Fig. 7. The spatial dissipation of the cloud as it propagates on its trajectory is clear, as well as a global trajectory that is increasingly radial.

Morphology and Brightness of the Modeled Dust Cloud. As the dust particles move farther from Fomalhaut, their individual scattered light fluxes drop; the spherical expansion of the cloud

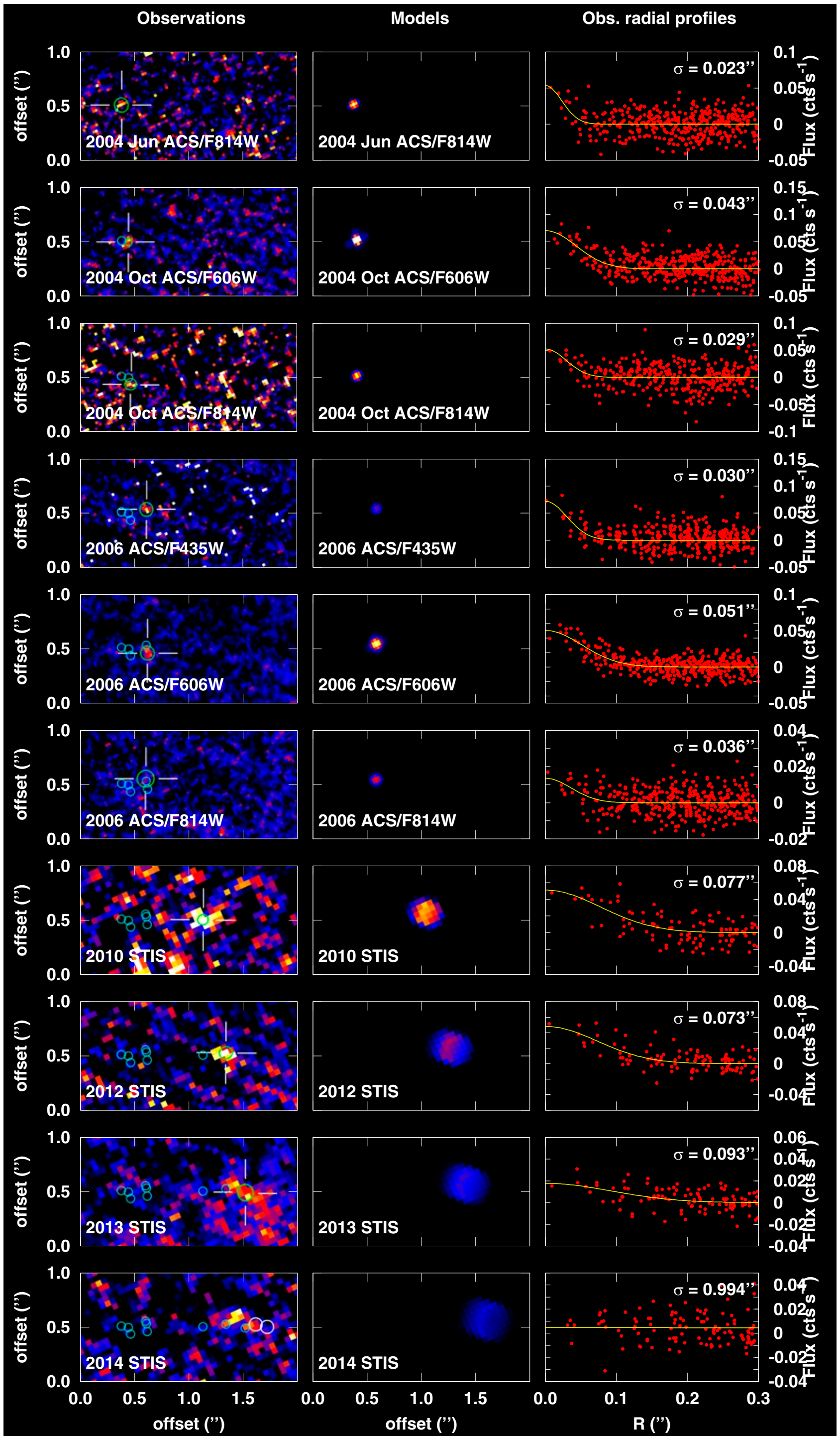

Fig. 7. Comparison of the evolution of the spatial scale, location, and surface brightness of the dust cloud as observed and modeled. The scaling of the images is the same as in Fig. 1 for both models (*Center* column) and observations (*Left* column). *Right* column also shows the fitted radial profiles of the observations. The radial profiles are corrected for instrumental effects in Fig. 8.

results in its overall surface brightness dropping as well. To simulate the observations, we convolved the model images with their appropriate ACS and STIS PSFs. The model images shown in Fig. 7 take into account the convolution and pixel sizes. We measured the fluxes in the model images using the same aperture radius and aperture corrections as we did for the data and then finally scaled the model to the observations.

The model predictions varied as a function of σ_{v}, the SD of the additional velocities of the daughter particles. The best fit was at $\sigma_{\mathrm{v}} = 0.13 \pm 0.01$ au·y^{-1}, which is 12% of the launch velocity and within 3 SD of the expansion slope fit. The results of the photometry of the model images, assuming this best-fitting σ_{v} value, are shown in Fig. 3. The correspondence between the modeled observations and the actual photometry is excellent. The PSF

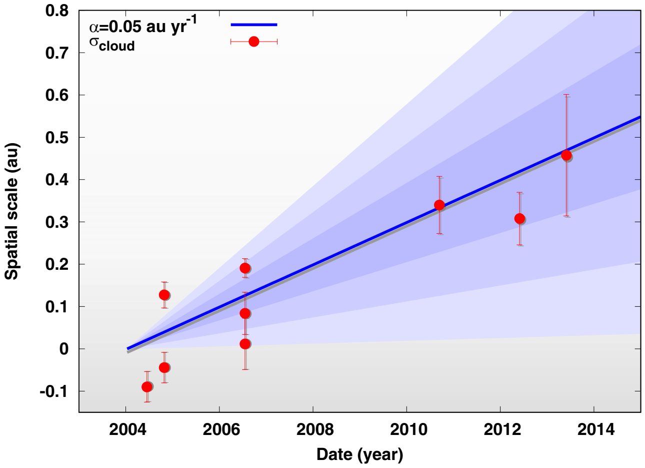

Fig. 8. The spatial evolution of the observed dust cloud and the best-fitting slope with a size increase of 0.05 ± 0.016 au·y^{-1}, which is ∼6.2% of the Keplerian velocity at the collisional location. We converted the observed radial profiles to spatial scales by subtracting the wavelength-dependent Gaussian of the HST PSFs from the observed profile widths and multiplying by the distance to the system. The shaded blue areas show the 1-, 2-, and 3σ regions of the fitting. The date intercept of the fit (and the estimated collision time) is at 2004.03 based on the expansion, only slightly earlier than predicted by the astrometric fits.

Table 4. Modeled position and brightness of the Fomalhaut b object

Date	Instrument	ΔR.A. (″)	Δδ (″)	F (Jy)
2004/06	ACS (F814W)	−8.583	9.153	3.925e-7
2004/10	ACS (F606W)	−8.593	9.187	5.605e-7
2004/10	ACS (F814W)			3.896e-7
2006/07	ACS (F435W)	−8.648	9.356	4.684e-7
2006/07	ACS (F606W)			4.811e-7
2006/07	ACS (F814W)			3.208e-7
2010/09	STIS	−8.836	9.822	3.907e-7
2012/05	STIS	−8.936	10.040	2.562e-7
2013/05	STIS	−9.000	10.174	1.885e-7
2014/09	STIS	−9.093	10.360	1.574e-7

The fluxes given were measured the same way as the observations and therefore may not yield the total modeled cloud flux. Positions are of the COM. 06, June; 10, October; 07, July; 09, September; 05, May.

convolutions and pixel rebinning, combined with the dissipation of the cloud, resulted in a higher peak in the STIS model images, just as observed. This is an observational artifact. The overall apparent decrease from 2004 to 2013 is a result of using photometry suitable for a point source on a source with increasing extent and decreasing surface brightness. Given the PSF subtraction artifacts in the image, photometry optimized to capture the full flux with a larger aperture is not possible. Based on the 2014 observations, our model, and the lack of HST measurements in subsequent years, future detection of the dust cloud is unlikely. In Table 4, we summarize the astrometry and photometry results of our best-fitting model.

Summary of Modeled Dust Cloud Dynamics. As a result of a catastrophic collision between two massive asteroids on the order of 100 km in radius, a short time prior to the first set of observations in 2004, a high surface density of dust particles ($\sim 4.8 \times 10^{22}$ cm^2) was produced in the Fomalhaut system. These dust particles represent the small end of a continuous distribution of fragments, up to tens of kilometers in radius. The fragments continue on the COM trajectory of the two asteroids, with a velocity of 1.09 au·y^{-1}, which is just slightly higher than the circular Keplerian solution of 0.89 au·y^{-1} at the location of the collision at 107 au. The explosive event disperses the fragments radially from the COM trajectory, with a variation of $\sigma_v = 0.13$ au·y^{-1}, which is 12% of the launch velocity and 15.5% of the local circular Keplerian solution. The smallest particles observed with HST in scattered light experience radiative forces, resulting in their increasingly radial trajectory.

Probability of Massive Collisions in the Fomalhaut System. Our photometry model indicates a dust cloud mass of $\sim 1.65 \times 10^{-8}\,\mathrm{M_{Earth}}$, integrating up to 1 mm in radius [assuming a density of 3.5 g·cm^{-3} appropriate for the likely composition (25)]. This equals a scattering surface area of 4.8×10^{22} cm^{-2}, assuming a simple πr^2 surface area of scattering. The exact total dust mass depends on the size distribution slope, which is why we also provide the scattering surface. Producing this amount of dust requires collisions of much more massive bodies. The required mass and size do not depend strongly on the nature of these bodies. Consolidated objects can fragment efficiently (34) with fragments extending up to 10 to 50 m in size (35, 36). Loosely bound rubble piles convey impact energy inefficiently (37) and have boulders up to similar sizes (38, 39) that will survive impact. Integrating the distributions from the smallest up to the largest fragments to determine total masses yields similar results for both cases.

How frequently would major collisions occur in the Fomalhaut system? We illustrate the answer by considering collisional outcomes and mutual collisional probabilities in a distribution of planetesimals. The total dust mass produced in the distribution of fragments in a single collision is

$$M_{\mathrm{fr}}(\mu, M) = \int_0^{Y(\mu,M)} A(\mu, M)\, m^{-\gamma+1} \mathrm{d}m, \qquad [2]$$

where μ is the mass of the smaller object, M is the mass of the larger object partaking in the collisional event that produced the distribution, and γ is the mass-distribution slope ($\alpha = 3\gamma - 2$). The variable Y gives the mass of the largest fragment in the continuous distribution (i.e., it is the second-largest fragment overall) and A is its scaling factor. The redistributed mass also equals the masses of the two colliding bodies, minus the overall largest fragment produced (X), which is not part of the continuous fragment distribution,

$$M_{\mathrm{fr}}(\mu, M) = \mu + M - X(\mu, M), \qquad [3]$$

allowing the scaling factor to be calculated. The values of X and Y are defined by the tensile strength of the bodies colliding, their sizes (masses), and their relative velocity. Depending on those factors, the collision will be either catastrophic (completely destroying both bodies) or only erosive. Our paper (28)

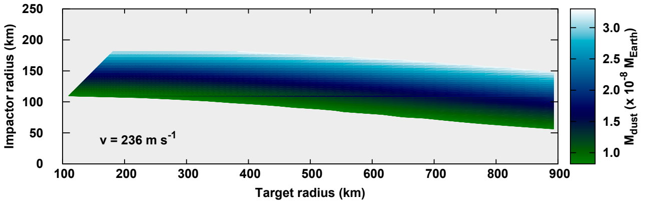

Fig. 9. The amount of dust produced up to radii of 1 mm as a function of the radii of the target and the impactor, assuming a collisional velocity of 236 m·s^{-1}. Domains producing 0.5 to 2 times the observed dust mass are shown.

discusses these collisional outcomes in more detail. For tensile strength, we assume the curve of ref. 40, traditionally used in debris disk cascade calculations. For the collisional speed, the expansion of the dust cloud provides a good estimate, as it will be roughly equal to the relative velocity of colliding bodies. The size of the cloud yields a collisional speed of 0.05 $\mathrm{au{\cdot}y^{-1}}$, while the photometric modeling results in 0.13 $\mathrm{au{\cdot}y^{-1}}$. These correspond to 236 and 616 $\mathrm{m{\cdot}s^{-1}}$, respectively. In Fig. 9, we show the dust mass (up to radii of 1 mm) produced in collisions between various target–impactor sizes at a collisional speed of 236 $\mathrm{m{\cdot}s^{-1}}$, in the domain where the produced dust mass is half to twice as much as is observed in the dust cloud. The smallest target capable of producing so much dust is 109 km in radius (when hit by a similar-size impactor); however, in erosive collisions, a 56-km body impacting an 893-km object can also generate this amount of dust. At the faster impact velocity, the catastrophic outcome remains approximately the same, while the erosive limit drops the impactor radius to 47 km. The escape velocity from the largest fragment in the catastrophic collision is $\sim$137 $\mathrm{m{\cdot}s^{-1}}$, suggesting a high impact velocity. However, the uncertainty in the expansion velocity is large and a larger impact velocity would not change our results.

The rate of collisions between planetesimals that could produce the required amount of dust depends on their number density and interaction velocity. Since Fomalhaut b is located near the inner edge of the Fomalhaut debris belt, we assume the density of parent bodies at the collisional location to be similar to that in the belt. We calculate the belt mass and density from its spectral energy distribution and thermal surface brightness, yielding a total of 26.15 $\mathrm{M_{Earth}}$, assuming a largest body in the distribution has a diameter of 2,000 km and that the belt material has a bulk density of 3.5 $\mathrm{g{\cdot}cm^{-3}}$. The timescale for collisional events producing the required amount of dust can be estimated by integrating the differential rate of collisions in the projectile and target mass space highlighted in Fig. 9. We integrate the domain that produces dust half of to double the amount observed, yielding timescales of $\sim$0.59 and $\sim$0.15 My for the 236 $\mathrm{m{\cdot}s^{-1}}$ and 616 $\mathrm{m{\cdot}s^{-1}}$ collisional velocities, respectively.

Fomalhaut b was above the detection level for only a decade, making it unlikely to have arisen in a dynamically cold quiescent planetary system given the timescales just derived. Even if the dust production is more efficient than we have assumed, i.e., the slope of the size-frequency distribution is steeper than -3.65, the rarity of this object is shown by the lack of similar sources among HST images of exoplanets and debris disks (41) compared with the near-infrared rate of true exoplanet detections (e.g., ref. 42).

Dynamical instability from planetary migration can stir planetesimal populations and increase their collision rates. It is the most likely explanation for events like Fomalhaut b and was also invoked by ref. 19. Such dynamical activity has been modeled in detail to explain the influence of planetary migration on the evolution of the solar system (43–45), leading to elevated planetesimal collision rates as reflected, for example, in the heavy bombardment indicated by the impact rate on the Moon (e.g., refs. 46–49).

Summary

The planetary nature of Fomalhaut b has been a mystery ever since its detection over a decade ago. In this paper, we present previously unpublished measurements of this object and also rereduce all archival data to present a coherent analysis that shows its behavior over a decade.

We find that the source has grown in extent since its discovery. We use updated astrometry and orbital solutions, finding its motion is consistent with radial (escaping) motion. To explain these observations, we model Fomalhaut b as an expanding dust cloud, containing copious amounts of dust produced in a massive planetesimal collision. Our model produces a light curve, angular extent, and orbital motion consistent with the observations spanning a decade. While Fomalhaut b is not likely to be a directly imaged exoplanet, it is probably an extraordinary supercatastrophic planetesimal collision observed in an exoplanetary system! Production of this amount of dust through planetesimal collisions in dynamically quiescent systems should be very rare. The rate of such events would be increased substantially if hypothetical planets around Fomalhaut are undergoing orbital migration, resulting in a dynamically active population of planetesimals.

Data Availability. The raw observational data can be downloaded from the MAST website maintained by the STScI. Our modeling code, DiskDyn, can be downloaded from https://github.com/merope82/DiskDyn.

ACKNOWLEDGMENTS. We are grateful for the hardware donation from Nvidia. We thank Paul Kalas for planning and obtaining the observations described here and our referees for providing helpful comments throughout the multiround review process. We also sincerely appreciate the postacceptance in-depth review of an independent HST/STIS expert. This work has been supported by NASA Exoplanets Research Program Grant 80NSSC20K0268 and NASA Grant 80NSSC18K0555.

1. P. Kalas *et al.*, Optical images of an exosolar planet 25 light-years from earth. *Science* **322**, 1345–1348 (2008).
2. C. Marois *et al.*, Direct imaging of multiple planets orbiting the star HR 8799. *Science* **322**, 1348–1352 (2008).
3. C. Marois, B. Zuckerman, Q. M. Konopacky, B. Macintosh, T. Barman, Images of a fourth planet orbiting HR 8799. *Nature* **468**, 1080–1083 (2010).
4. T. S. Barman, B. Macintosh, Q. M. Konopacky, C. Marois, Clouds and chemistry in the atmosphere of extrasolar planet HR8799b. *Astrophys. J.* **733**, 65–82 (2011).
5. T. Currie *et al.*, A combined subaru/VLT/MMT 1-5 μm study of planets orbiting HR 8799: Implications for atmospheric properties, masses, and formation. *Astrophys. J.* **729**, 128 (2011).
6. M. S. Marley *et al.*, Masses, radii, and cloud properties of the HR 8799 planets. *Astrophys. J.* **754**, 135 (2012).
7. A. Zurlo *et al.*, First light of the VLT planet finder SPHERE. III. New spectrophotometry and astrometry of the HR 8799 exoplanetary system. *Astron. Astrophys.* **587**, A57 (2016).
8. M. Marengo *et al.*, Spitzer/infrared array camera limits to planetary companions of Fomalhaut and epsilon Eridani. *Astrophys. J.* **700**, 1647–1657 (2009).
9. E. Chiang, E. Kite, P. Kalas, J. R. Graham, M. Clampin, Fomalhaut's debris disk and planet: Constraining the mass of Fomalhaut b from disk morphology. *Astrophys. J.* **693**, 734–749 (2009).
10. E. E. Mamajek, On the age and binarity of Fomalhaut. *Astrophys. J.* **754**, L20 (2012).
11. M. Janson *et al.*, Infrared non-detection of Fomalhaut b: Implications for the planet interpretation. *Astrophys. J.* **747**, 116 (2012).
12. M. Janson *et al.*, High-contrast imaging with spitzer: Deep observations of Vega, Fomalhaut, and ϵ Eridani. *Astron. Astrophys.* **574**, A120 (2015).
13. P. Kalas, J. R. Graham, M. P. Fitzgerald, M. Clampin, STIS coronagraphic imaging of Fomalhaut: Main belt structure and the orbit of Fomalhaut b. *Astrophys. J.* **775**, 56 (2013).
14. H. Beust *et al.*, An independent determination of Fomalhaut b's orbit and the dynamical effects on the outer dust belt. *Astron. Astrophys.* **561**, A43 (2014).
15. G. M. Kennedy, M. C. Wyatt, Collisional evolution of irregular satellite swarms: Detectable dust around solar system and extrasolar planets. *Mon. Not. R. Astron. Soc.* **412**, 2137–2153 (2011).
16. T. Currie *et al.*, Direct imaging confirmation and characterization of a dust-enshrouded candidate exoplanet orbiting Fomalhaut. *Astrophys. J.* **760**, L32 (2012).
17. R. Galicher, C. Marois, B. Zuckerman, B. Macintosh, Fomalhaut b: Independent analysis of the Hubble space telescope public archive data. *Astrophys. J.* **769**, 42 (2013).
18. S. J. Kenyon, T. Currie, B. C. Bromley, Fomalhaut b as a cloud of dust: Testing aspects of planet formation theory. *Astrophys. J.* **786**, 70 (2014).
19. S. M. Lawler, S. Greenstreet, B. Gladman, Fomalhaut b as a dust cloud: Frequent collisions within the Fomalhaut disk. *Astrophys. J.* **802**, L20 (2015).
20. S. J. Kenyon, B. C. Bromley, Collisional cascade calculations for irregular satellite swarms in Fomalhaut b. *Astrophys. J.* **811**, 60 (2015).
21. D. Tamayo, Consequences of an eccentric orbit for Fomalhaut b. *Mon. Not. R. Astron. Soc.* **438**, 3577–3586 (2014).

22. J. R. Walsh, P. Goudfrooij, E. Malumuth, "STIS geometric distortion - SMOV3A tests for CCD, NUVMAMA and FUV-MAMA" (STIS Instrument Science Report 2001-02, Space Telescope Science Institute, Baltimore, MD, 2001).
23. J. E. Krist, R. N. Hook, F. Stoehr, "20 years of Hubble space telescope optical modeling using tiny tim" in *Optical Modeling and Performance Predictions V*, M. A. Kahan, Ed. (SPIE, 2011), vol. 8127, pp. 166–181.
24. D. Foreman-Mackey, D. W. Hogg, D. Lang, J. Goodman, Emcee: The MCMC hammer. *Publ. Astron. Soc. Pac.* **125**, 306–312 (2013).
25. N. P. Ballering, K. Y. L. Su, G. H. Rieke, A. Gáspár, A comprehensive dust model applied to the resolved beta pictoris debris disk from optical to radio wavelengths. *Astrophys. J.* **823**, 108 (2016).
26. T. Waza, T. Matsui, K. Kani, Laboratory simulation of planetesimal collision. II - Ejecta velocity distribution. *J. Geophys. Res.* **90**, 1995–2011 (1985).
27. J. J. Lissauer, G. R. Stewart, "Growth of planets from planetesimals" *in Protostars and Planets III*, E. H. Levy, J. I. Lunine, Eds. (University of Arizona Press, Tucson, AZ, 1993), pp. 1061–1088.
28. A. Gáspár, D. Psaltis, F. Özel, G. H. Rieke, A. Cooney, Modeling collisional cascades in debris disks: The numerical method. *Astrophys. J.* **749**, 14 (2012).
29. D. Nesvorný, D. Vokrouhlický, W. F. Bottke, M. Sykes, Physical properties of asteroid dust bands and their sources. *Icarus* **181**, 107–144 (2006).
30. F. Moreno *et al.*, The dust environment of comet 67P/Churyumov-Gerasimenko from Rosetta OSIRIS and VLT observations in the 4.5 to 2.9 AU heliocentric distance range inbound. *Astron. Astrophys.* **587**, A155 (2016).
31. F. Moreno, J. Licandro, A. Cabrera-Lavers, F. J. Pozuelos, Early evolution of disrupted asteroid P/2016 G1 (PANSTARRS). *Astrophys. J.* **826**, L22 (2016).
32. F. Moreno, J. Licandro, A. Cabrera-Lavers, F. J. Pozuelos, Dust loss from activated asteroid P/2015 X6. *Astrophys. J.* **826**, 137 (2016).
33. J. C. Weingartner, B. T. Draine, Dust grain-size distributions and extinction in the Milky Way, large Magellanic cloud, and small Magellanic cloud. *Astrophys. J.* **548**, 296–309 (2001).
34. C. El Mir, K. Ramesh, D. C. Richardson, A new hybrid framework for simulating hypervelocity asteroid impacts and gravitational reaccumulation. *Icarus* **321**, 1013–1025 (2019).
35. D. D. Durda *et al.*, Size-frequency distributions of fragments from SPH/N-body simulations of asteroid impacts: Comparison with observed asteroid families. *Icarus* **186**, 498–516 (2007).
36. M. Jutzi, P. Michel, D. C. Richardson, Fragment properties from large-scale asteroid collisions: I: Results from SPH/N-body simulations using porous parent bodies and improved material models. *Icarus* **317**, 215–228 (2019).
37. P. G. Benavidez *et al.*, Impact simulation in the gravity regime: Exploring the effects of parent body size and internal structure. *Icarus* **304**, 143–161 (2018).
38. T. Michikami *et al.*, Size-frequency statistics of boulders on global surface of asteroid 25143 Itokawa. *Earth Planets Space* **60**, 13–20 (2008).
39. T. Michikami *et al.*, Boulder size and shape distributions on asteroid Ryugu. *Icarus* **331**, 179–191 (2019).
40. W. Benz, E. Asphaug, Catastrophic disruptions revisited. *Icarus* **142**, 5–20 (1999).
41. A. M. Hughes, G. Duchêne, B. C. Matthews, Debris disks: Structure, composition, and variability. *Annu. Rev. Astron. Astrophys.* **56**, 541–591 (2018).
42. K. Wagner, D. Apai, K. M. Kratter, On the mass function, multiplicity, and origins of wide-orbit giant planets. *Astrophys. J.* **877**, 46 (2019).
43. R. Gomes, H. F. Levison, K. Tsiganis, A. Morbidelli, Origin of the cataclysmic late heavy bombardment period of the terrestrial planets. *Nature* **435**, 466–469 (2005).
44. R. G. Strom, R. Malhotra, T. Ito, F. Yoshida, D. A. Kring, The origin of planetary impactors in the inner solar system. *Science* **309**, 1847–1850 (2005).
45. H. F. Levison, A. Morbidelli, K. Tsiganis, D. Nesvorný, R. Gomes, Late orbital instabilities in the outer planets induced by interaction with a self-gravitating planetesimal disk. *Astron. J.* **142**, 152 (2011).
46. R. Malhotra, M. Holman, T. Ito, Chaos and stability of the solar system. *Proc. Natl. Acad. Sci. U.S.A.* **98**, 12342–12343 (2001).
47. Y. Wu, Y. Lithwick, Secular chaos and the production of hot Jupiters. *Astrophys. J.* **735**, 109 (2011).
48. M. B. Davies *et al.*, "The long-term dynamical evolution of planetary systems" *in Protostars and Planets VI*, H. Beuther, R. S. Klessen, C. P. Dullemond, T. Henning, Eds. (University of Arizona Press, Tucson, AZ, 2014), pp. 787–808.
49. A. Morbidelli *et al.*, The timeline of the lunar bombardment: Revisited. *Icarus* **305**, 262–276 (2018).